

1 **Methodology to determine the coupling of continental clouds with surface and**
2 **boundary layer height under cloudy conditions from lidar and meteorological**
3 **data**

4

5 Tianning Su¹, Youtong Zheng², and Zhanqing Li¹

6

7 ¹Department of Atmospheric and Oceanic Sciences & ESSIC, University of Maryland
8 , College Park, Maryland 20740, USA

9 ²The Program in Atmospheric and Oceanic Sciences, Princeton University, and
10 NOAA/Geophysical Fluid Dynamics Laboratory, Princeton, NJ, USA

11

12

13

14

15

16

17

18 *Correspondence to:* Zhanqing Li (zhanqing@umd.edu)

19 Tianning Su (tianning@umd.edu)

20 **Abstract.** The states of coupling between clouds and surface or boundary-layer have
21 been investigated much more extensively for marine stratocumulus clouds than for
22 continental low clouds, partly due to more complex thermodynamic structures over land.
23 A manifestation is a lack of robust remote sensing methods to identify coupled and
24 decoupled clouds over land. Following the idea for determining cloud coupling over
25 the ocean, we have generalized the concept of coupling and decoupling to low clouds
26 over land, based on potential temperature profiles. Furthermore, by using ample
27 measurements from lidar and a suite of surface meteorological instruments at the U.S.
28 Department of Energy's Atmospheric Radiation Measurement Program's Southern
29 Great Plains site from 1998 to 2019, we have developed a method to simultaneously
30 retrieve the planetary boundary layer (PBL) height (PBLH) and coupled states under
31 cloudy conditions during the daytime. The new lidar-based method relies on the PBLH,
32 the lifted condensation level, and the cloud base to diagnose the cloud coupling. The
33 coupled states derived from this method are highly consistent with those derived from
34 radiosondes. Retrieving the PBLH under cloudy conditions that has been a persistent
35 problem in lidar remote sensing, is resolved in this study. Our method can lead to high-
36 quality retrievals of the PBLH under cloudy conditions, and the determination of cloud
37 coupling states. With the new method, we find that coupled clouds are sensitive to
38 changes in the PBL with a strong diurnal cycle, whereas decoupled clouds and the PBL
39 are weakly related. Since coupled and decoupled clouds have distinct features, our new
40 method offers an advanced tool to separately investigate them in climate systems.

41 **1 Introduction**

42 A large fraction of low clouds is driven by surface fluxes through the conduits of
43 the planetary boundary layer (PBL) over land (e.g., Betts, 2009; Ek and Holtslag, 2004;
44 Golaz et al., 2002; Teixeira and Hogan, 2002; Zheng et al., 2020; Wei et al., 2020;
45 Santanello et al., 2018). This is a coupled cloud-surface system (Cheruy et al., 2014;
46 Zheng and Rosenfeld, 2015; Wu et al., 1998). However, not all low clouds respond to
47 surface forcing. Those clouds without close interactions with the local surface are
48 considered to be in a decoupled state. Given that the PBL is, by definition, the lowest
49 atmospheric layer influenced by the underlying surface (Stull, 1988), to what degree
50 the PBL top overlaps with cloud bases becomes a good criterion to separate coupled
51 and decoupled low clouds.

52 Conventionally, the “coupled state” of a cloud-topped marine boundary layer
53 implies that the moist conserved variables are vertically well mixed within the PBL
54 (Bretherton and Wyant, 1997; Dong et al., 2015; Zheng and Li, 2019; Zheng et al.,
55 2018). However, such a definition cannot be simply applied to clouds over land since
56 the definition and the determination methods of the PBL over land differ from those
57 over ocean (Garratt, 1994; Vogelezang and Holtslag, 1996). The concept of coupled and
58 decoupled states is typically used to characterize marine stratocumulus clouds due to
59 their large-scale coverages (Nicholls, 1984). Since stratocumulus only constitutes a
60 relatively small portion of continental clouds (Warren et al., 1986), we attempt to extend
61 the concept of coupling and decoupling to characterize low clouds over land. Due to
62 the relatively complex thermodynamics, the moisture conserved variables (e.g., total

63 water mixing ratio and liquid potential temperature) may not be a constant in the
64 coupled sub-cloud layer (Driedonks, 1982; Stull, 1988).

65 Following parcel theory, the lifted condensation level (LCL) has been used to
66 diagnose a coupled cloud, based on the distance between the LCL and the cloud base
67 (e.g., Dong et al., 2015; Glenn et al., 2020; Zheng and Rosenfeld, 2015; Zheng et al.,
68 2020). When potential temperature and humidity are uniformly distributed in the
69 vertical, the LCL should be consistent with the cloud base for coupled cases. However,
70 the cloud base for coupled cases can considerably differ from the LCL over land
71 because potential temperature and humidity have large variabilities in the vertical scale
72 within the PBL over land (Driedonks, 1982; Guo et al., 2016; Stull, 1988; Su et al.,
73 2017a). To address the limitation in the LCL method, we attempt to develop a remote
74 sensing method to distinguish coupled and decoupled clouds over land.

75 Since the PBL height (PBLH) is the maximum height directly influenced by surface
76 fluxes, we consider coupling with the PBL equivalent to coupling with the land surface.
77 Thus, we use the PBLH as a critical parameter to diagnose the coupling between clouds
78 and the land surface. The degree of coupling may thus be gauged in terms of
79 quantitative differences between the cloud base and the PBL top. Such differences can
80 be determined in a height coordinate system or in a potential temperature coordinate
81 system (Kasahara, 1974). For this purpose, ground-based lidar has great potential
82 because it can continuously track the development of the PBL (Demoz et al., 2006;
83 Hageli et al., 2000; Sawyer and Li, 2013; Su et al., 2017b) and clouds (Clothiaux et al.,
84 2000; Platt et al., 1994; Zhao et al., 2014) at high temporal and vertical resolutions.

85 By jointly using lidar measurements and meteorological data from the U.S.
86 Department of Energy's Atmospheric Radiation Measurement (ARM) Southern Great
87 Plains (SGP) site (36.6°N, 97.48°W), we attempt to identify coupled and decoupled low
88 clouds during the daytime. Unlike previous studies that use the LCL or radiosonde (RS)
89 data to diagnose coupled clouds (e.g., Dong et al., 2015; Zheng and Rosenfeld, 2015),
90 this study developed a lidar-based method to determine the status of cloud coupling
91 over land at a high temporal resolution.

92 The paper is organized as follows. Section 2 describes the measurements and data.
93 Section 3 describes the new methodology in terms of the definition and implementation.
94 The performance of the method is demonstrated in Section 4, and a summary is
95 presented in Section 5.

96

97 **2 Data Descriptions**

98 *2.1 Radiosonde*

99 RS launches took place at least four times per day at the ARM SGP site, usually at
100 0030, 0630, 1230, and 1830 local time (LT). Holdridge et al. (2011) provide technical
101 details about the ARM RS (<https://www.arm.gov/capabilities/instruments/sonde>). In
102 this study, we consistently use daylight saving time (Coordinated Universal Time -5 h)
103 as local time throughout the year to avoid inconsistencies between summer and winter.
104 Besides the routine measurements, there are fewer, but still considerable numbers of
105 RS data obtained at other times of the day (e.g., 0930, 1200, 1300, 1530, and 1900 LT).

106 These supplemental RS samples at other times comprise ~10% of the total number of
107 cases. RS data from 0630–1900 LT are utilized in this study. The vertical resolution of
108 RS data varies according to the rising rate of the balloon, but measurements are
109 generally taken ~10 m apart. We further vertically average the RS data to achieve a
110 vertical resolution of 5 hPa.

111 There are several methods to determine PBLH from RS-measured temperature,
112 pressure, and humidity profiles. They include, among others, the parcel method
113 (Holzworth, 1964), the gradient methods (Stull, 1988; Seidel et al., 2010), and the
114 Richardson number method (Vogelezang and Holtslag, 1996). After examining the
115 previous methods, Liu and Liang (2010) proposed a different approach to determine the
116 PBLH that is valid under different thermodynamic conditions. The robust performance
117 was demonstrated over the SGP site and in other major field campaign sites around the
118 world (Liu and Liang, 2010). Thus, we adopted this method to calculate PBLH from
119 RS data in this study. The potential temperature is corrected as the virtual potential
120 temperature, θ_v , using the water vapor mixing ratio [WVMR; $\theta_v = (1 + 0.61 \text{WVMR})$].
121 The virtual potential temperature does not include a correction for the liquid water
122 content profile, as this is challenging to measure in many conditions. Therefore, the
123 virtual potential temperature is not conserved during moist convection. Since we mainly
124 focus on the sub-cloud atmosphere, this is not a serious problem. Moreover, we use
125 scaled RS moisture profiles normalized by the total precipitable water vapor derived
126 from the microwave radiometer (<https://www.arm.gov/capabilities/vaps/lssonde>,
127 Revercomb et al., 2003).

128

129 *2.2 Micropulse lidar (MPL) system*

130 MPL backscatter profiles were collected at the SGP site from September 1998 to
131 July 2019 with high continuity (Campbell et al., 2002). Technical details and data
132 availability can be found at the website
133 <https://www.arm.gov/capabilities/instruments/mpl>. The backscatter profiles have a
134 vertical resolution of 30 m. MPL signals have an initial temporal resolution of 10–30 s
135 and are averaged every 10 min for this study. Due to the inherent problem of lidar
136 observations, there is a ~0.2-km near-surface “blind zone”. Following the standard
137 lidar-data processing, background subtraction, signal saturation and overlapping, after-
138 pulse and range corrections are applied to the raw MPL data (Campbell et al., 2002,
139 2003). Questionable data are excluded based on the quality-control flags.

140

141 *2.3 Cloud product*

142 The MPL can be used to detect cloud layers based on signal gradients (Platt et al.,
143 1994). Lidar-based methods are accurate for determining the cloud-base height (CBH)
144 but may miss information about the cloud top due to the signal saturation within an
145 optically thick cloud (Clothiaux et al., 2000). Under this condition, the cloud radar
146 provides a better estimation of the cloud-top height (CTH). In this study, we directly
147 use an existing quality-controlled cloud product, CLDTYPE/ARSCL
148 (<https://www.arm.gov/capabilities/vaps/cldtype>), which combines information from

149 the MPL, ceilometer, and cloud radar to determine the vertical boundaries of clouds
150 (Clothiaux et al., 2000; Flynn et al., 2017). For the lowest cloud base, the best
151 estimation from laser-based techniques (i.e., MPL and ceilometer) is used. The original
152 temporal resolution of the CLDTYPE/ARSCL product is 1 min, averaged to a 10-min
153 temporal resolution. To avoid averaging jumps in signal between different clouds, a
154 cloud is considered to be continuous if its base height varies less than 0.25 km between
155 two consecutive profiles.

156

157 **3 Methodology**

158 *3.1 Definition of coupled and decoupled clouds based on thermodynamics*

159 The definition of the state of cloud-surface coupling over land is a critical question.
160 For marine stratocumulus, coupled clouds are identified when the liquid water potential
161 temperature varies less than a certain threshold (i.e., 0.5 K) below the cloud base (Jones
162 et al., 2011). We try to extend the concept of coupling and decoupling to clouds over
163 land. The PBL over land is typically buoyancy driven and controlled by surface fluxes
164 during the daytime. We consider a cloud is in the coupled state when it strongly interacts
165 with the buoyancy fluxes within the PBL.

166 Figure 1 presents the idealized vertical profiles of virtual potential temperature (θ_v)
167 under the clear-sky, coupled cloud, and decoupled cloud. A superadiabatic surface layer
168 exchanges the heat fluxes between the surface and PBL. The outer layer and
169 entrainment zone are turbulently coupled with the surface, and thus, are considered as

170 the coupled regime. Meanwhile, the free atmosphere is considered as the decoupled
171 regime. Theoretically, θ_v is constant in the outer layer, and follows the wet adiabatic
172 lapse rate in the cloud layer. Although the profiles of θ_v in the real atmosphere can
173 largely differ from the idealized profiles, the relative position between the cloud layer
174 and capping inversion of entrainment zone is clear. For the coupled cases, the cloud
175 base is below the capping inversion of entrainment zone. For the decoupled cases, the
176 cloud base is above the capping inversion. Based on this feature, we can use the profiles
177 of virtual potential temperature (θ_v) in the sub-cloud layer to determine the coupling
178 state of continental clouds. It should be noted that the virtual potential temperature is
179 not conserved in a moist adiabatic process and thus would decrease within a cloud layer.
180 On the other hand, the liquid potential temperature remains a near-constant within the
181 stratocumulus. Since we use the profiles of potential temperature in the sub-cloud layer
182 to diagnose the cloud coupling, there is no difference in the identification results by
183 using the virtual potential temperature.

184 Following the previous studies (Jones et al., 2011; Dong et al., 2015), we attempt
185 to use the variations in the potential temperature within the sub-cloud layer to diagnose
186 the cloud coupling. For determining a suitable threshold, we first look at several
187 examples of profiles of θ_v and WVMR from the RS (Figure 2). If the CBH is lower
188 than the PBLH, the cloud is affected by turbulence and buoyancy fluxes in the PBL,
189 such as the cases shown in Figure 2a. Note that the PBLH is not an absolute boundary
190 limiting turbulence and buoyancy fluxes. Due to the overshooting of rising air parcels,
191 we use a range to screen the condition of coupled clouds. As shown in Figure 2b, even

192 when the CBH is slightly above the PBLH, WVMR and θ_v are still relatively
193 consistent between the cloud layer and the PBL and show large step signals at the cloud
194 top.

195 Figure 2c-d shows a clear inversion layer between the cloud base and the PBL top,
196 and the difference in θ_v between the CBH and the PBLH ($\Delta\theta_v$) is relatively large.
197 Such a notable inversion layer prevents the buoyancy fluxes within the PBL from
198 reaching the cloud base, leading to the decoupling between the cloud and the PBL.
199 Overall, we consider $\Delta\theta_v$ as the key factor to determine cloud coupling. In Figure 2,
200 $\Delta\theta_v$ for coupled cases (a-c) is -0.32 K and 0.31 K, respectively, and $\Delta\theta_v$ for
201 decoupled cases (d-e) is 1.47 K and 5.0 K, respectively.

202 Therefore, instead of giving a height range to limit the differences between CBH
203 and PBLH, we consider using the differences in θ_v between CBH and PBLH to
204 determine the threshold for distinguishing coupled and decoupled clouds. For
205 convenience, we use $\Delta\theta_v$ to refer to the difference in θ_v between the CBH and the
206 PBLH ($\Delta\theta_v = \theta_v^{\text{CBH}} - \theta_v^{\text{PBLH}}$). For decoupled cases, the cloud base is above the
207 capping inversion of entrainment zone. There is a notable inversion in θ_v between
208 PBL top and decoupled cloud base. Thus, we identify the cases satisfying $\Delta\theta_v > \delta_s$ as
209 being in a decoupled state. Correspondingly, we identify the cases satisfying $\Delta\theta_v < \delta_s$
210 as being in a coupled state. We set the range of CBH to between 0 and 4 km and
211 excluded cases of deep convection (i.e., $\text{CBH} < 4$ km and $\text{CTH} > 6.5$ km). In the
212 previous studies for marine clouds, the difference in the potential temperature between
213 the CBH and the near-surface is used as the criterion (Jones et al., 2011; Dong et al.,

214 2015). However, we use the potential temperature at the PBL top instead of the potential
215 temperature near the surface. This change is due to the relatively complex
216 thermodynamic structure over the land. The large variation in the potential temperature
217 within the surface layer would notably affect the result. Hence, we use the potential
218 temperature above the PBL top to replace those values near the surface.

219 As the basic framework of PBL, the slab model assumes that θ_v is constant within
220 the PBL (Wallace and Hobbs, 2006). Under this assumption, δ_s can be set as 0.
221 However, there are certain variations in θ_v within the PBL, which can cause inversions
222 with relatively small magnitudes between the cloud base and PBL top. Figure 3a
223 presents the inversion strength in θ_v within PBL during the daytime. Specifically,
224 inversions represent the layers with continuously increased structures of θ_v . For an
225 inversion layer, the inversion strength is calculated as the differences in θ_v between the
226 top and bottom of the layer. The inversions near surface or across the PBL top are
227 excluded. Besides the capping inversion and surface inversion, the inversion strength
228 within PBL is typically below 1K. Therefore, we set δ_s as 1 K, which is the same as
229 the criterion for determining stable or convective conditions (Liu and Liang, 2010).
230 Furthermore, we demonstrate the probability density function (PDF) of $\Delta\theta_v$ for the
231 low cloud cases. Coupled and decoupled clouds are classified by the threshold of δ_s
232 (1 K). Through the development of PBL, boundary layer clouds frequently occur in the
233 entrainment zone, and form a coupled cloud-PBL system. For such coupled systems,
234 θ_v at cloud top and PBL top is highly consistent for the majority of cases. Thus, the
235 PDF of $\Delta\theta_v$ shows significantly high values for the range of -2 K to 0.5 K in the

236 coupled regime. Meanwhile, the PDF of $\Delta\theta_v$ is evenly distributed in the decoupled
237 regime. Since we only analyze low clouds, the PDF of $\Delta\theta_v$ slowly decrease when $\Delta\theta_v$
238 is above 10 K.

239 Based on the variations in θ_v within PBL, we set δ_s as 1 K. However, it should
240 note that it is not an absolute value. A similar threshold of 0.5 K has been used for
241 marine stratocumulus (Jones et al., 2011; Dong et al., 2015). Comparing to the marine
242 condition, θ_v show greater variabilities over land. Hence, the threshold is
243 correspondingly larger. On the other hand, since the threshold of 1 K is in the low PDF
244 regime (Figure 3b), the small changes in this value would not notably affect the
245 identifications. Specifically, a 0.1 K difference in δ_s will lead to a 0.5% difference in
246 the identification of coupled cloud.

247 Same to the previous studies (Jones et al., 2010; Dong et al., 2015; Zheng and
248 Rosenfeld, 2015), we identified the coupled clouds as the thermodynamics coupling
249 between surface and cloud base. However, it is an open question whether the entire
250 cloud layer is coupled for coupled cases. It depends on whether the liquid water
251 potential temperature is conserved within the cloud layer, which represents a moisture
252 adiabatic process. This issue is closely related to the cloud types. In the cloud
253 parameterizations, the entire stratocumulus layer is considered to be well-mixed,
254 while the cumulus-capped layer is usually partially mixed (Lock, 2000). For
255 stratocumulus clouds, the entire cloud layer and PBL are typically fully coupled with
256 surface, when the cloud base is coupled with surface. For the cumulus-capped PBL, the
257 entire cloud layer may not be completely coupled, despite the coupling between cloud

258 base and surface. The well-established parameterizations are supported by many
259 observational studies (e.g., Betts, 1986; Storer et al., 2015; Berkes et al., 2016, de Roode
260 and Wang, 2006; Ott et al., 2009).

261

262 *3.2 Lidar-based method to identify coupled and decoupled clouds*

263 *3.2.1 Method description*

264 Given the rapid change in clouds over land, RS observations have limitations when
265 it comes to tracking cloud development due to the coarse temporal resolution and
266 drifting of the balloon. We thus further developed a lidar-based method to identify the
267 coupled states of clouds based on our new algorithm for retrieving the PBLH that can
268 better track the diurnal variations in PBLH than conventional lidar-based approaches
269 (Su et al., 2020). We adapted this algorithm for retrieving the PBLH and developed a
270 new scheme to deal with cloudy conditions. Following the original method (Su et al.
271 2020), the rainy cases are eliminated in the quality control process. The principles
272 behind the PBLH algorithm are stated next for completeness.

273 Our new PBLH algorithm can retrieve the PBL variability from the MPL under
274 Different Thermo-Dynamic Stability (thus named the DTDS algorithm) conditions,
275 taking into account the vertical coherence and temporal continuity of the PBLH. First,
276 we identify the local maximum positions (LMPs; range: 0.25–4 km) in profiles of the
277 wavelet covariance transform function derived from lidar backscatter (Brooks, 2003).
278 These LMPs are the potential positions of the PBLH. We can use the PBLH derived

279 from morning RS soundings as the starting point. Without morning RS soundings, the
280 algorithm can still work well, with the lowest LMPs selected as the starting point, which
281 reduces by 0.02–0.05 the correlation coefficient between MPL-derived and RS-derived
282 PBLHs (Su et al., 2020).

283 To ensure good continuity, we select the closest LMP to the earlier position of the
284 PBLH. Different stages of PBL development are considered. DTDS-derived PBLHs
285 likely increase during the growth stage and decrease during the decaying stage, but the
286 algorithm is also able to identify decreases during the growth stage or increases during
287 the decaying stage based on the selection scheme described by Su et al. (2020). There
288 are multiple step signals in the backscatter profiles when complex aerosol structures
289 (e.g., the residual layer) are present, leading to multiple LMPs. Based on temporal
290 continuity, we select the appropriate LMP as the position of the PBL top. However,
291 PBLH retrievals still suffer from relatively low accuracies under stable conditions
292 because of the weak vertical mixing and residual layer.

293 Clouds induce strong step signals in the lidar backscatter, further considerably
294 affecting PBLH retrievals. Su et al. (2020) only considered cases where the low cloud
295 top coincided with the previous PBL top, excluding other low-cloud cases (> 60% of
296 all low-cloud cases). Here, we specifically consider coupled and decoupled states of
297 low clouds. Due to the MPL's ~0.2-km blind zone, we only analyze the PBLH and CBH
298 above 0.2 km. Figure 4 presents the flow chart describing the updated DTDS algorithm.
299 In particular, we jointly use PBL development and the LCL to diagnose the states of
300 coupling or decoupling. In ideal situations, LCL, PBLH, and CBH are highly consistent

301 with each other for coupled clouds. But for real conditions, we only require that either
302 the LCL or the PBLH coincides with the CBH for identifying coupled cases, with
303 another parameter serving as an additional constraint. Specifically, a coupled cloud
304 needs to occur within a certain range of LCL and the previous position of the PBL top.

305 For the DTDS algorithm, five empirical parameters are used, including A_1 , A_2 ,
306 A_3 , A_4 , A_5 . As listed in the Table 1, $A_1 - A_5$ are set as 0.7, 0.2, 0.15, 1.35, and 1.1,
307 respectively. A cloud at time i is identified as being in the coupled state if the CBH is
308 less than $[H(i - 1) + 0.2 \text{ km } (A_2)]$ and $[\text{LCL} + 0.7 \text{ km } (A_1)]$. This step moves 39.5%
309 of low cloud cases to the category of decoupled clouds. A cloud is also considered to
310 be in a coupled state if the CBH is coincident with the LCL within 0.15 km (A_3), and
311 the CBH is less than $[H(i - 1) + 0.7 \text{ km } (A_1)]$, where $H(i - 1)$ represents the
312 PBLH at time $(i - 1)$. This step further moves 17.8% of the remaining cases to the
313 category of decoupled clouds.

314 The LCL is calculated from surface meteorological data (relative humidity,
315 temperature, pressure) at the SGP site based on an exact expression (Romps, 2017).
316 Specifically, Romps. (2017) proposed an exact, explicit, analytic expression for LCL as
317 a function of surface meteorology. Compared to the previous approximate expressions,
318 some of which may have an uncertainty in the order of hundreds of meters, the Romps
319 expression can be considered as the precise value. The uncertainty of empirical vapor
320 pressure data may lead to a bias of ~ 5 -m (Romps, 2017), which may be neglected in the
321 analyses.

322 After determining the coupling or decoupling state of a cloud, we retrieve $H(i)$

323 (i.e., PBLH at time i) based on the cloud state. For decoupled cases, we use the same
324 strategy for a clear sky to retrieve the PBLH. Based on the selection scheme in the
325 DTDS algorithm, the LMP below the CBH is selected as $H(i)$. For coupled cases, we
326 jointly use CBH and CTH to determine PBLH. During the warm season, active cumulus
327 often occurs in the upper part of the PBL with strong surface heating, so the CBH can
328 be generally regarded as the PBLH (Stull, 1988; Wallace and Hobbs, 2006). Under this
329 condition, the CBH coincides with the previous PBL top. Therefore, if $[CTH \geq$
330 $PBLH_{30min} + 0.2 km (A_2)]$, we set $H(i) = A_5 CBH$, where $PBLH_{30min}$ is the
331 average value of the PBLH within 30 min of the prior time i . Hence, A_5 would be a
332 critical parameter for the PBLH estimation. On the other hand, if $[CTH <$
333 $PBLH_{30min} + 0.2 km (A_2)]$, we set $H(i)$ equal to the minimum between CTH and the
334 product $A_4 * CBH$. This step is designed for thin clouds or some stratiform clouds. In
335 particular, $A_5 * CBH$ can be notably larger than the CTH for a thin cloud. Under this
336 situation, we tend to use CTH to denote the PBL top. This step has little impact on the
337 detection of surface-cloud coupling, but can assure that the CTH of the coupled cloud
338 is always higher than the retrieved PBLH to fit the real situation.

339 After retrieving $H(i)$, we consider that the cloud above the PBLH is still coupled
340 if $[CBH < H(i) + 0.2 km (A_2)]$. Moreover, we added an upper limit for all PBLH
341 retrievals. If $[H(i) > LCL + 0.7 km (A_1)]$, we adjust $H(i)$ as the maximum LMP
342 below the LCL. The new DTDS method combines lidar measurements and surface
343 meteorological observations and can simultaneously retrieve the PBLH and cloud states.

344

345 3.2.2 Selection of empirical parameters

346 The states of coupling and decoupling are diagnostic parameters rather than explicit
347 expressions. Similar to the other methods for retrieving PBLH (e.g., Brooks, 2003; Liu
348 and Liang, 2010), multiple empirical parameters are used to determine PBLH. Table 1
349 lists the five empirical parameters in the algorithm. These parameters are related with
350 three factors, including LCL, PBLH, CBH. The sensitivity to the selection of these
351 parameters is presented. The detailed impacts of variations in these parameters on the
352 retrievals of cloud coupling and PBLH will be discussed in this section.

353 Note that we used the CTH and $A_4 * CBH$ as the upper limits for PBLH retrievals in
354 the DTDS algorithm. For coupled cases, these two limits are generally close to or above
355 the position of the PBL top. Only 2% (3%) of total cases meet the condition that the
356 RS-derived PBLH is 0.25 km higher than the CTH ($A_4 * CBH$). Section 4 presents the
357 detailed relationships between CBH, CTH, and PBLH. In the DTDS method, CTH
358 serves as the upper limit for PBLH under the condition of coupled shallow cumulus.

359 Similar to previous studies, we can also use the LCL as the standard to identify
360 coupled clouds (Dong et al., 2015; Zheng and Rosenfeld, 2015). We assume a cloud is
361 coupled if $|CBH - LCL| < \Delta h$. By using ~ 7500 RS profiles, the cloud coupling state
362 derived from the virtual potential temperature method (Section 3.1) is considered as the
363 ground truth for evaluation. Figure 5a shows the commission errors and omission errors
364 for different criteria. Here, the commission error is calculated as the percentage of
365 decoupled clouds misidentified as coupled clouds. The commission error can also be
366 called a “false positive”, as the former is a common term for describing the nature of

367 an error in identification. The omission error is calculated as the percentage of coupled
368 clouds that have not been identified under this criterion. By using the LCL, we can
369 obtain a relatively low commission error if the criterion is less than 0.15 km and a
370 relatively low omission error if the criterion is greater than 0.7 km. Thus, we set A_1
371 and A_3 as 0.7 and 0.15 in the DTDS method to exclude and to select cases of coupled
372 clouds. We can also use the RS-derived PBLH as the criterion (Figure 5b).

373 Despite the coarse temporal resolution, the RS-derived PBLH can be a good
374 criterion to use to distinguish between coupling and decoupling. If we consider a
375 coupled cloud as a cloud where ($CBH < RS\text{-derived PBLH} + 0.2 \text{ km}$), both commission
376 and omission errors are $\sim 5\%$. Therefore, we primarily use [$PBLH + 0.2 \text{ km}$ (A_2)] in the
377 DTDS method to identify coupled and decoupled regimes. As cloud can considerably
378 affect with lidar backscattering and generate large signal variations, we jointly use lidar
379 backscattering, the previous position of PBL top, and LCL to determine the surface-
380 cloud coupling and PBLH. In particular, the LCL constraint in the algorithm notably
381 reduces the absolute biases in PBLH retrievals under cloudy conditions by 9.3%.

382 Moreover, we test the sensitivity of selecting these empirical parameters. Figure 6
383 presents the commission errors and omission errors in the identifications of coupled
384 clouds for selecting different values of empirical parameters. Among these parameters,
385 A_2 is the critical one, which would notably affect the identification results. In general,
386 A_2 determine the maximum differences between PBLH and CBH for coupled cases. If
387 [$CBH - PBLH > A_2$], we consider the cloud is under the decoupled state. Thus, the
388 identification method is quite sensitive to A_2 . Selecting a low value of A_2 would

389 neglect many coupled cases, which leads to a high omission error. Meanwhile, selecting
390 a high value of A_2 would misclassify many coupled cases, which leads to a high
391 commission error. After a trail and error, A_2 is set as 0.2 km to balance the omission
392 and commission errors. The selections for other parameters are not sensitive for the
393 coupled cloud identifications. We can choose them from a reasonable range.

394 As a by-product of this method, we also pay attentions to the PBLH retrievals under
395 cloudy conditions. Figure 7 presents the mean absolute biases and correlation
396 coefficients between PBLH derived from lidar and radiosonde for selecting different
397 values of empirical parameters. To match the scope of this study, we only analyze the
398 low cloud conditions. For retrieving PBLH under cloudy conditions, A_2 is the critical
399 parameter. The variations in correlation coefficients under different values of empirical
400 parameters are small with a range of 0.81-0.82. However, the absolute biases can
401 considerably differ under different values of A_5 . In general, A_5 represents the ratio
402 between CBH and PBLH under coupled conditions. If A_5 is above 1.1, PBLH
403 retrievals under cloudy conditions are overestimated. We set A_5 as 1.1 to achieve a
404 relatively low bias and a relatively high correlation coefficient at the same time. For
405 other parameters, the selections from reasonable ranges would not notably affect the
406 PBLH retrievals.

407 In short, selections of these empirical parameters are based on the overall
408 relationship between cloud and PBL under the coupled and decoupled states. In our
409 method, the selection of A_2 is critical for the identifications of coupled clouds, while
410 the selection of A_5 is critical for the PBLH retrievals under cloudy conditions. The

411 selections of other parameters are not sensitive.

412

413 **4 Results**

414 Figure 8 illustrates four examples of PBLH retrievals and cloud states derived from
415 the DTDS algorithm for 27 October 2011, 31 July 2002, 19 March 2000, and 1 May
416 2012. Figure 8a depicts coupled shallow cumulus occurring at noontime at the PBL top.
417 With a weak surface flux of $\sim 200 \text{ W m}^{-2}$, this shallow cumulus cloud appeared for less
418 than an hour. Figure 8b shows a developed coupled cumulus cloud. With a strong
419 surface flux of $\sim 500 \text{ W m}^{-2}$, this coupled cloud continuously developed during the
420 daytime. Figure 8c presents the case of a daylong coupled cloud. After the passage of a
421 frontal system that day, stratocumulus occurred during the morning with a cloud
422 thickness of 0.5 km. Through the development of the PBL, the thick stratocumulus
423 cloud was broken up by the strong turbulences, transforming into shallow cumulus
424 clouds. Figure 8d shows the case of an active coupled cloud, which is generally
425 associated with a large amount of convective available potential energy. Even though
426 coupled clouds can differ in appearance and variability throughout the day, the common
427 feature is the coherent variation between the cloud base and the PBL top. The LCL is a
428 relevant parameter and can differ from the PBLH and the CBH for some coupled cases
429 (e.g., Figure 8b-c).

430 The identification accuracy, or disparity between different methods, are evaluated
431 in terms of the selected criteria, for which the identification method based on $\Delta\theta_v$ is
432 regarded as the “truth”, as described in Section 3.1. Hereafter, all results are analyzed

433 for the period of 1000–1900 LT, so early-morning data are not used. The commission
434 error is 10.1%, and the omission error is 6.8% for the DTDS method. Note that lidar-
435 based PBLH methods generally suffer from relatively low accuracy under stable
436 atmospheric conditions. Following Liu and Liang (2010), we identified stable PBLs
437 from RS measurements. Since coupled clouds are driven by relatively strong buoyancy
438 fluxes, only 1% of total cases of coupled clouds occurred under stable PBL conditions
439 during the study period (0700–1900 LT). Therefore, the relatively low accuracy for
440 stable PBLs is not a major problem in this study.

441 Figure 5 also compares the accuracy between the DTDS and LCL methods. Based
442 on the LCL alone, we cannot choose an appropriate criterion to achieve a lower
443 commission error and omission error simultaneously. Thus, we do not use the LCL as
444 the single standard to detect the coupling and decoupling of low clouds in our study. As
445 diagnostic parameters, different methods inevitably produce different results regarding
446 coupling and decoupling. Although we consider the method based on $\Delta\theta_v$ as the
447 standard, it still suffers from uncertainties arising from balloon drifting. From this
448 perspective, it is hard to conclude which method is the best. Since it determines the
449 PBLH based on aerosol backscattering, the lidar-based method may be more
450 representative of the coupling between a cloud and the aerosol layer near the surface
451 when clear skies occur, at least during a short window of time.

452 Figure 9a-b presents the occurrence frequencies of the CBH and the CTH at
453 different heights. Despite the same variation ranges, clouds are mostly coupled if the
454 CBH is lower than 1 km, while decoupled clouds dominate if the CBH is higher than 3

455 km. Figure 9c-d shows the changes in the coupled fraction (ratio of coupled cases to
456 total cases) with different CBHs and CTHs. The coupled fraction is about 90% if the
457 CBH is lower than 1 km and decreases to 2% for CBHs above 3 km. Although the CBHs
458 for coupled cases are generally less than 3 km, CTHs for coupled cases can be much
459 higher. Coupled clouds still account for around 10% of the cases with CTHs above 6
460 km.

461 Figure 10 shows scatter plots between CBH, CTH, PBLH, and LCL for coupled
462 and decoupled clouds. For coupled clouds, there is a generally strong correlation
463 between CBH, LCL, and PBLH, contrary to the weak relationships of decoupled cases.
464 The relationship between CTH and RS-derived PBLH is complicated. For shallow
465 cumulus clouds, their tops can be considered as PBL tops for the coupled state, while
466 the cloud top is considerably above the position of the PBL top for active cumulus
467 clouds. We also note that the accuracy of CTH retrievals is generally lower than the
468 accuracy of CBH retrievals (Clothiaux et al., 2000). As CTH is not a criterion for cloud
469 coupling, the accuracy of CTH would not affect the identification of coupled cloud, but
470 may affect the PBLH retrievals for the coupled cloud cases. Meanwhile, despite the
471 laser-based detection of CBH is considered as the standard method (Platt et al., 1994;
472 Clothiaux et al., 2000; Lim et al., 2019), the CBH retrievals from ceilometer or lidar
473 still bear some uncertainties, which can potentially lead to a mean bias of 0.1 km (Silber
474 et al., 2018; Cromwell et al., 2019). In our method, a systematic increase of 0.1 km in
475 the CBH can lead to an increase of 2.1% in omission errors and a decrease of 1% in
476 commission errors.

477 After identifying the coupling state of clouds, it is feasible to retrieve the PBLH
478 under cloudy conditions. In particular, the DTDS-derived PBLH needs to resort to the
479 cloud position for coupled cloud cases. For decoupled cloud cases, on the other hand,
480 the PBLH below clouds is sought to avoid cloud interference. For coupled clouds,
481 DTDS-derived PBLHs show a strong correlation with RS-derived PBLHs with a
482 correlation coefficient (R) of ~ 0.9 (Figure 10d). For decoupled cases, the correlation
483 between DTDS-derived PBLHs and RS-derived PBLHs is generally good (R = 0.73)
484 but worse than the correlation for coupled cases (Figure 10h). As pointed out in previous
485 studies (Chu et al., 2019; Hageli et al., 2000; Lewis et al., 2013; Su et al., 2017b), it has
486 been a persistent problem to retrieve the PBLH under cloudy conditions since the strong
487 backscattering and step signals from cloud interference would be excluded to avoid
488 interfering with the retrievals. The PBLH determined by our method under a cloudy
489 condition is much more reasonable. Moreover, due to the different definitions of the
490 PBLH and aerosol stratification within the PBL, there are always considerable
491 differences between lidar- and RS-derived PBLHs, which cannot be eliminated by a
492 specific algorithm (Chu et al., 2019; Su et al., 2020).

493

494 **5 Summary**

495 In this study, we proposed a novel method for distinguishing between coupled and
496 decoupled low clouds over land. Based on the understanding of PBL processes and
497 quantitative analyses, we developed a lidar-based method (DTDS) to identify the
498 coupling state of low clouds over the SGP site. In practice, we identified a coupled

499 cloud when the position of the cloud base was generally close to or lower than the
500 previous position of the PBL top, with the LCL serving as an additional restriction.
501 Compared to using the LCL alone, the coupled states identified by the DTDS method
502 show better consistency with the results derived from radiosondes, with about 10%
503 differences between the lidar-based retrievals and radiosonde results.

504 Not only coupled state, also retrieved by the method is the PBLH under cloudy
505 conditions. A long-lasting problem with lidar-retrieval of PBLH is either incapability
506 of retrieval or large uncertainties induced by the occurrence of low clouds (e.g., Chu et
507 al., 2019; Hageli et al., 2000; Lewis et al., 2013), we address this issue by separately
508 considering the coupled and decoupled of low clouds. Specifically, in coupled
509 conditions, the position of the coupled cloud serves as a good reference for identifying
510 the PBLH. In decoupled conditions, the large backscatter and step signals from clouds
511 would be excluded to avoid interfering with the retrievals. With our method, cloudy
512 conditions are well handled.

513 With the new method, we study the difference of cloud-PBL interactions in coupled
514 and decoupled conditions. In contrast to the sensitive responses of coupled clouds to
515 changes in the PBLH and buoyancy, the decoupled clouds and the PBLH are weakly
516 related. Due to their different relationships with the PBL, a robust distinguishment
517 between the coupled and decoupled low clouds is critical for further investigating the
518 coupled land-atmosphere system and aerosol-cloud interactions. Our methodology
519 paves a solid ground for such pursuits.

520

521 *Data availability.* All these datasets are publicly available at the ARM archive
522 https://adc.arm.gov/discovery/#/results/site_code::sgp. The products developed in this
523 study, i.e., cloud states and the PBLH, are currently available upon request from the
524 lead author (tianning@umd.edu) and are expected to be added to the ARM archive in
525 the near future.

526

527 *Author contribution.* T.S., Y.Z., and Z.L. conceptualized this study. T.S. carried out the
528 analysis, with comments from other co-authors. T.S., Y.Z., and Z.L. interpreted the data
529 and wrote the manuscript.

530

531 *Competing interests.* The authors declare that they have no conflict of interest.

532

533 *Acknowledgements.* This work was supported by grants from the U.S. Department of
534 Energy (DE-SC0018996), the National Science Foundation (AGS1837811), and NASA
535 (NNX16AN61G). We acknowledge the provision of radiosonde, MPL data, surface
536 meteorological data, and cloud products by the U.S. Department of Energy's ARM
537 program. We thank the two anonymous reviewers for their comments.

538

539 **References**

540 Berkes, F., Hoor, P., Bozem, H., Kunkel, D., Sprenger, M. and Henne, S. (2016).

541 Airborne observation of mixing across the entrainment zone during PARADE 2011.
542 Atmospheric Chemistry and Physics, 16(10), pp.6011-6025.

543 Betts, A.K. (2009). Land-surface-atmosphere coupling in observations and models.
544 *Journal of Advances in Modeling Earth Systems*, 1(3).
545 <https://doi.org/10.3894/JAMES.2009.1.4>

546 Bretherton, C. S., and Wyant, M. C. (1997). Moisture transport, lower-tropospheric
547 stability, and decoupling of cloud-topped boundary layers. *Journal of the*
548 *Atmospheric Sciences*, 54(1), 148–167. [https://doi.org/10.1175/1520-](https://doi.org/10.1175/1520-0469(1997)054<0148:MTL TSA>2.0.CO;2)
549 [0469\(1997\)054<0148:MTL TSA>2.0.CO;2](https://doi.org/10.1175/1520-0469(1997)054<0148:MTL TSA>2.0.CO;2)

550 Brooks, I. M. (2003). Finding boundary layer top: application of a wavelet covariance
551 transform to lidar backscatter profiles. *Journal of Atmospheric and Oceanic*
552 *Technology*, 20, 1092–1105. [https://doi.org/10.1175/1520-](https://doi.org/10.1175/1520-0426(2003)020<1092:FBLT AO>2.0.CO;2)
553 [0426\(2003\)020<1092:FBLT AO>2.0.CO;2](https://doi.org/10.1175/1520-0426(2003)020<1092:FBLT AO>2.0.CO;2)

554 Campbell, J. R., Hlavka, D. L., Welton, E. J., Flynn, C. J., Turner, D. D., Spinhirne, J.
555 D., ... Hwang, I. H. (2002). Full-time, eye-safe cloud and aerosol lidar
556 observation at atmospheric radiation measurement program sites: instruments and
557 data processing. *Journal of Atmospheric and Oceanic Technology*, 19(4), 431–442.
558 [https://doi.org/10.1175/1520-0426\(2002\)019<0431:FTESCA>2.0.CO;2](https://doi.org/10.1175/1520-0426(2002)019<0431:FTESCA>2.0.CO;2)

559 Campbell, J.R., Welton, E.J., Spinhirne, J.D., Ji, Q., Tsay, S.C., Piketh, S.J., Barenbrug,
560 M. and Holben, B.N., 2003. Micropulse lidar observations of tropospheric aerosols
561 over northeastern South Africa during the ARREX and SAFARI 2000 dry season

562 experiments. *Journal of Geophysical Research: Atmospheres*, 108(D13).

563 Cheruy, F., Dufresne, J. L., Hourdin, F., and Ducharne, A. (2014). Role of clouds and
564 land-atmosphere coupling in midlatitude continental summer warm biases and
565 climate change amplification in CMIP5 simulations. *Geophysical Research Letters*,
566 41(18), 6493–6500. <https://doi.org/10.1002/2014GL061145>

567 Chu, Y., Li, J., Li, C., Tan, W., Su, T., and Li, J. (2019). Seasonal and diurnal variability
568 of planetary boundary layer height in Beijing: intercomparison between MPL and
569 WRF results. *Atmospheric Research*, 227, 1–13.
570 <https://doi.org/10.1016/j.atmosres.2019.04.017>

571 Clothiaux, E. E., Ackerman, T. P., Mace, G. G., Moran, K. P., Marchand, R. T., Miller,
572 M. A., and Martner, B. E. (2000). Objective determination of cloud heights and
573 radar reflectivities using a combination of active remote sensors at the ARM CART
574 sites. *Journal of Applied Meteorology*, 39(5), 645–665.
575 [https://doi.org/10.1175/1520-0450\(2000\)039<0645:ODOCHA>2.0.CO;2](https://doi.org/10.1175/1520-0450(2000)039<0645:ODOCHA>2.0.CO;2)

576 Cromwell, E., and Flynn, D. (2019). Lidar cloud detection with fully convolutional
577 networks. In 2019 IEEE Winter Conference on Applications of Computer Vision
578 (WACV) (pp. 619-627). IEEE.

579 de Roode, S.R. and Wang, Q. (2007). Do stratocumulus clouds detrain? FIRE I data
580 revisited. *Boundary-layer meteorology*, 122(2), pp.479-491.

581 Demoz, B., Flamant, C., Weckwerth, T., Whiteman, D., Evans, K., Fabry, F., and
582 Schwemmer, G. (2006). The dryline on 22 May 2002 during IHOP_2002:

583 convective-scale measurements at the profiling site. *Monthly Weather Review*,
584 134(1), 294–310. <https://doi.org/10.1175/MWR3054.1>

585 Dong, X., Schwantes, A. C., Xi, B., and Wu, P. (2015). Investigation of the marine
586 boundary layer cloud and CCN properties under coupled and decoupled conditions
587 over the Azores. *Journal of Geophysical Research: Atmospheres*, 120, 6179–6191.
588 <https://doi.org/10.1002/2014JD022939>

589 Driedonks, A. G. M. (1982). Models and observations of the growth of the atmospheric
590 boundary layer. *Boundary-Layer Meteorology*, 23(3), 283–306.
591 <https://doi.org/10.1007/BF00121117>

592 Ek, M. B., and Holtslag, A. A. M. (2004). Influence of soil moisture on boundary layer
593 cloud development. *Journal of Hydrometeorology*, 5(1), 86–99.
594 [https://doi.org/10.1175/1525-7541\(2004\)005<0086:IOSMOB>2.0.CO;2](https://doi.org/10.1175/1525-7541(2004)005<0086:IOSMOB>2.0.CO;2)

595 Flynn, D., Shi, Y., Lim, K., and Riihimaki, L. (2017). Cloud Type Classification
596 (cldtype) Value-Added Product. Ed. by Robert Stafford, ARM Research Facility.
597 DOE/SC-ARM-TR-200.

598 Garratt, J. R. (1994). Review: the atmospheric boundary layer. *Earth-Science Reviews*,
599 37(1-2), 89–134. [https://doi.org/10.1016/0012-8252\(94\)90026-4](https://doi.org/10.1016/0012-8252(94)90026-4)

600 Glenn, I. B., Feingold, G., Gristey, J. J., and Yamaguchi, T. (2020). Quantification of
601 the radiative effect of aerosol-cloud-interactions in shallow continental cumulus
602 clouds. *Journal of the Atmospheric Sciences*, 77, 2905–2920.
603 <https://doi.org/10.1175/JAS-D-19-0269.1>

604 Golaz, J. C., Larson, V. E., and Cotton, W. R. (2002). A PDF-based model for boundary
605 layer clouds. Part I: Method and model description. *Journal of the Atmospheric*
606 *Sciences*, 59(24), 3540–3551. [https://doi.org/10.1175/1520-](https://doi.org/10.1175/1520-0469(2002)059<3540:APBMFB>2.0.CO;2)
607 [0469\(2002\)059<3540:APBMFB>2.0.CO;2](https://doi.org/10.1175/1520-0469(2002)059<3540:APBMFB>2.0.CO;2)

608 Guo, J., Miao, Y., Zhang, Y., Liu, H., Li, Z., Zhang, W., ... Zhai, P. (2016). The
609 climatology of planetary boundary layer height in China derived from radiosonde
610 and reanalysis data. *Atmospheric Chemistry and Physics*, 16(20), 13,309–13,319.
611 <https://doi.org/10.5194/acp-16-13309-2016>

612 Hageli, P., Steyn, D. G., and Strawbridge, K. B. (2000). Spatial and temporal variability
613 of mixed-layer depth and entrainment zone thickness. *Boundary-Layer*
614 *Meteorology*, 97, 47–71. <https://doi.org/10.1023/A:1002790424133>

615 Holdridge, D., Ritsche, M., Prell, J., and Coulter, R. (2011). Balloon-borne sounding
616 system (SONDE) handbook. <https://www.arm.gov/capabilities/instruments/sonde>

617 Holzworth, G. C., (1964). Estimates of mean maximum mixing depths in the contiguous
618 United States, *Mon. Weather Rev.*, 92, 235–242, [https://doi.org/10.1175/1520-](https://doi.org/10.1175/1520-0493(1964)092<0235:eommmmd>2.3.co;2)
619 [0493\(1964\)092<0235:eommmmd>2.3.co;2](https://doi.org/10.1175/1520-0493(1964)092<0235:eommmmd>2.3.co;2).

620 Jones, C., Bretherton, C., and Leon, D. (2011). Coupled vs. decoupled boundary layers
621 in VOCALS-REx. *Atmospheric Chemistry and Physics*, 11(14), 7143–7153.
622 <https://doi.org/10.5194/acp-11-7143-2011>

623 Kasahara, A. (1974). Various vertical coordinate systems used for numerical weather
624 prediction. *Monthly Weather Review*, 102(7), 509–522.

625 [https://doi.org/10.1175/1520-0493\(1974\)102<0509:VVCSUF>2.0.CO;2](https://doi.org/10.1175/1520-0493(1974)102<0509:VVCSUF>2.0.CO;2)

626 Lewis, J. R., Welton, E. J., Molod, A. M., and Joseph, E. (2013). Improved boundary
627 layer depth retrievals from MPLNET. *Journal of Geophysical Research:*
628 *Atmospheres*, 118(17), 9870–9879. <https://doi.org/10.1002/jgrd.50570>

629 Lim, K.S.S., Riihimaki, L.D., Shi, Y., Flynn, D., Kleiss, J.M., Berg, L.K., Gustafson,
630 W.I., Zhang, Y. and Johnson, K.L. (2019). Long-term retrievals of cloud type and
631 fair-weather shallow cumulus events at the ARM SGP site. *Journal of Atmospheric*
632 *and Oceanic Technology*, 36(10), pp.2031-2043.

633 Liu, S. Y., and Liang, X. Z. (2010). Observed diurnal cycle climatology of planetary
634 boundary layer height. *Journal of Climate*, 23, 5790–5809.
635 <https://doi.org/10.1175/2010JCLI3552.1>

636 Lock, A. P., Brown, A. R., Bush, M. R., Martin, G. M., & Smith, R. N. B. (2000). A
637 new boundary layer mixing scheme. Part I: Scheme description and single-column
638 model tests. *Monthly weather review*, 128(9), 3187-3199.

639 Nicholls, S. (1984). The dynamics of stratocumulus: aircraft observations and
640 comparisons with a mixed layer model. *Quarterly Journal of the Royal*
641 *Meteorological Society*, 110(466), 783–820.
642 <https://doi.org/10.1002/qj.49711046603>

643 Ott, L. E., Bacmeister, J., Pawson, S., Pickering, K., Stenchikov, G., Suarez, M., ... and
644 Xueref-Remy, I. (2009). Analysis of convective transport and parameter sensitivity
645 in a single column version of the Goddard earth observation system, version 5,

646 general circulation model. *Journal of the Atmospheric Sciences*, 66(3), 627-646.

647 Platt, C. M., Young, S. A., Carswell, A. I., Pal, S. R., McCormick, M. P., Winker, D.
648 M., ... and Wooldridge, C. (1994). The Experimental Cloud Lidar Pilot Study
649 (ECLIPS) for cloud-radiation research. *Bulletin of the American Meteorological*
650 *Society*, 75, 1635–1654. [https://doi.org/10.1175/1520-](https://doi.org/10.1175/1520-0477(1994)075<1635:TECLPS>2.0.CO;2)
651 [0477\(1994\)075<1635:TECLPS>2.0.CO;2](https://doi.org/10.1175/1520-0477(1994)075<1635:TECLPS>2.0.CO;2)

652 Revercomb, H.E., Turner, D.D., Tobin, D.C., Knuteson, R.O., Feltz, W.F., Barnard, J.,
653 Bösenberg, J., Clough, S., Cook, D., Ferrare, R. and Goldsmith, J., 2003. The ARM
654 program's water vapor intensive observation periods: Overview, initial
655 accomplishments, and future challenges. *Bulletin of the American Meteorological*
656 *Society*, 84(2), pp.217-236.

657 Romps, D. M. (2017). Exact expression for the lifting condensation level. *Journal of*
658 *the Atmospheric Sciences*, 74(12), 3891–3900. [https://doi.org/10.1175/JAS-D-17-](https://doi.org/10.1175/JAS-D-17-0102.1)
659 [0102.1](https://doi.org/10.1175/JAS-D-17-0102.1)

660 Santanello Jr., J. A., Dirmeyer, P. A., Ferguson, C. R., Findell, K. L., Tawfik, A. B.,
661 Berg, A., ... and Roundy, J. (2018). Land–atmosphere interactions: the LoCo
662 perspective. *Bulletin of the American Meteorological Society*, 99(6), 1253–1272.
663 <https://doi.org/10.1175/BAMS-D-17-0001.1>

664 Sawyer, V., and Li, Z. Q. (2013). Detection, variations and intercomparison of the
665 planetary boundary layer depth from radiosonde, lidar and infrared spectrometer.
666 *Atmospheric Environment*, 79, 518–528.

667 <https://doi.org/10.1016/j.atmosenv.2013.07.019>

668 Seidel, D. J., Ao, C. O., and Li, K. (2010). Estimating climatological planetary boundary layer
669 heights from radiosonde observations: Comparison of methods and uncertainty analysis.
670 *Journal of Geophysical Research: Atmospheres*, 115(D16).

671 Silber, I., J. Verlinde, E. W. Eloranta, C. J. Flynn, and D. M. Flynn (2018), Polar liquid
672 cloud base detection algorithms for high spectral resolution or micropulse lidar data,
673 *J. Geophys. Res.: Atmos.*, doi: 10.1029/2017JD027840.

674 Storer, R.L., Griffin, B.M., Höft, J., Weber, J.K., Raut, E., Larson, V.E., Wang, M. and
675 Rasch, P.J. (2015). Parameterizing deep convection using the assumed probability
676 density function method. *Geoscientific Model Development*, 8(1), pp.1-19.

677 Stull, R. B. (1988). *An Introduction to Boundary Layer Meteorology*. Dordrecht:
678 Springer Netherlands.

679 Su, T., Li, J., Li, C. C., Xiang, P. Z., Lau, A. K. H., Guo, J. P., ... and Miao, Y. C. (2017b).
680 An intercomparison of long-term planetary boundary layer heights retrieved from
681 CALIPSO, ground-based lidar, and radiosonde measurements over Hong Kong.
682 *Journal of Geophysical Research: Atmospheres*, 122, 3929–3943.
683 <https://doi.org/10.1002/2016JD025937>

684 Su, T., Li, J., Li, J., Li, C., Chu, Y., Zhao, Y., ... Wang, L. (2017a). The evolution of
685 springtime water vapor over Beijing observed by a high dynamic Raman lidar
686 system: case studies. *IEEE Journal of Selected Topics in Applied Earth
687 Observations and Remote Sensing*, 10(5), 1715–1726.

688 <https://doi.org/10.1109/JSTARS.2017.2653811>

689 Su, T., Li, Z., and Kahn, R. (2018). Relationships between the planetary boundary layer
690 height and surface pollutants derived from lidar observations over China: regional
691 pattern and influencing factors. *Atmospheric Chemistry and Physics*, 18(21),
692 15,921–15,935. <https://doi.org/10.5194/acp-18-15921-2018>

693 Su, T., Li, Z., and Kahn, R. (2020). A new method to retrieve the diurnal variability of
694 planetary boundary layer height from lidar under different thermodynamic stability
695 conditions. *Remote Sensing of Environment*, 237, 111519.
696 <https://doi.org/10.1016/j.rse.2019.111519>

697 Teixeira, J., and Hogan, T. F. (2002). Boundary layer clouds in a global atmospheric
698 model: simple cloud cover parameterizations. *Journal of Climate*, 15(11), 1261–
699 1276. [https://doi.org/10.1175/1520-0442\(2002\)015<1261:BLCIAG>2.0.CO;2](https://doi.org/10.1175/1520-0442(2002)015<1261:BLCIAG>2.0.CO;2)

700 M. (1996). Evaluation and model impacts of alternative boundary-layer height
701 formulations. *Boundary-Layer Meteorology*, 81(3-4), 245–269.
702 <https://doi.org/10.1007/BF02430331>

703

704 Wallace, J. M., and Hobbs, P. V. (2006). *Atmospheric Science: an Introductory Survey*.
705 Amsterdam, Boston: Elsevier Academic Press.

706 Warren, G., Hahn, C. J., London, J., Chervin, M., and Jenne, R. L. (1986). Global
707 distribution of total cloud cover and cloud type amounts over land. (Rep. DOE/ER-
708 0406). Washington, DC: U.S. DOE Office of Energy Research.

709 Wei, J., Huang, W., Li, Z., Sun, L., Zhu, X., Yuan, Q., Liu, L. and Cribb, M., 2020.
710 Cloud detection for Landsat imagery by combining the random forest and
711 superpixels extracted via energy-driven sampling segmentation approaches.
712 Remote Sensing of Environment, 248, p.112005.

713 Welton, E. J., Campbell, J. R., Spinhirne, J. D., and Scott III, V. S. (2001). Global
714 monitoring of clouds and aerosols using a network of micropulse lidar systems. In
715 *Lidar Remote Sensing for Industry and Environment Monitoring* (Vol. 4153, 151–
716 158). International Society for Optics and Photonics.

717 Wu, X., Grabowski, W. W, and Moncrieff, M. W. (1998). Long-term behavior of cloud
718 systems in TOGA COARE and their interactions with radiative and surface
719 processes. Part I: Two-dimensional modeling study. *Journal of the Atmospheric*
720 *Sciences*, 55(17), 2693–2714. [https://doi.org/10.1175/1520-
721 0469\(1998\)055<2693:LTBOCS>2.0.CO;2](https://doi.org/10.1175/1520-0469(1998)055<2693:LTBOCS>2.0.CO;2)

722 Yang, D., Li, C., Lau, A. K. H., and Li, Y. (2013). Long-term measurement of daytime
723 atmospheric mixing layer height over Hong Kong. *Journal of Geophysical*
724 *Research: Atmospheres*, 118(5), 2422–2433. <https://doi.org/10.1002/jgrd.50251>

725 Yang, T., Wang, Z., Zhang, W., Gbaguidi, A., Sugimoto, N., Wang, X., Matsui, I. and
726 Sun, Y., 2017. Boundary layer height determination from lidar for improving air
727 pollution episode modeling: development of new algorithm and evaluation.
728 Atmospheric Chemistry and Physics, 17(10), p.6215.

729 Zhao, C., Wang, Y., Wang, Q., Li, Z., Wang, Z., and Liu, D. (2014). A new cloud and

730 aerosol layer detection method based on micropulse lidar measurements. *Journal*
731 *of Geophysical Research: Atmospheres*, 119(11), 6788–6802.
732 <https://doi.org/10.1002/2014JD021760>

733 Zheng, Y., and Li, Z. (2019). Episodes of warm-air advection causing cloud-surface
734 decoupling during the MARCUS. *Journal of Geophysical Research: Atmospheres*,
735 124(22). <https://doi.org/10.1029/2019JD030835>

736 Zheng, Y., and Rosenfeld, D. (2015). Linear relation between convective cloud base
737 height and updrafts and application to satellite retrievals. *Geophysical Research*
738 *Letters*, 42(15), 6485–6491. <https://doi.org/10.1002/2015GL064809>

739 Zheng, Y., Rosenfeld, D., and Li, Z. (2018). Estimating the decoupling degree of
740 subtropical marine stratocumulus decks from satellite. *Geophysical Research*
741 *Letters*, 45. <https://doi.org/10.1029/2018GL078382>

742 Zheng, Y., Sakradzija, M., Lee, S.-S., and Li, Z. (2020). Theoretical understanding of
743 the linear relationship between convective updrafts and cloud-base height for
744 shallow cumulus clouds. Part II: Continental conditions. *Journal of the*
745 *Atmospheric Sciences*, 77, 1313–1328. <https://doi.org/10.1175/JAS-D-19-0301.1>

746

747 **Tables**

748 **Table 1. List of parameters in the flow chart of DTDS (Figure 4).**

	Unit	Related factors	Value	Sensitivity (coupled states)	Sensitivity (PBLH)
A_1	km	LCL / PBLH	0.7	Low	Low
A_2	km	PBLH	0.2	High	Low
A_3	km	LCL	0.15	Low	Low
A_4	dimensionless	CBH	1.35	Low	Low
A_5	dimensionless	CBH	1.1	Low	High

749

750

751

752

753

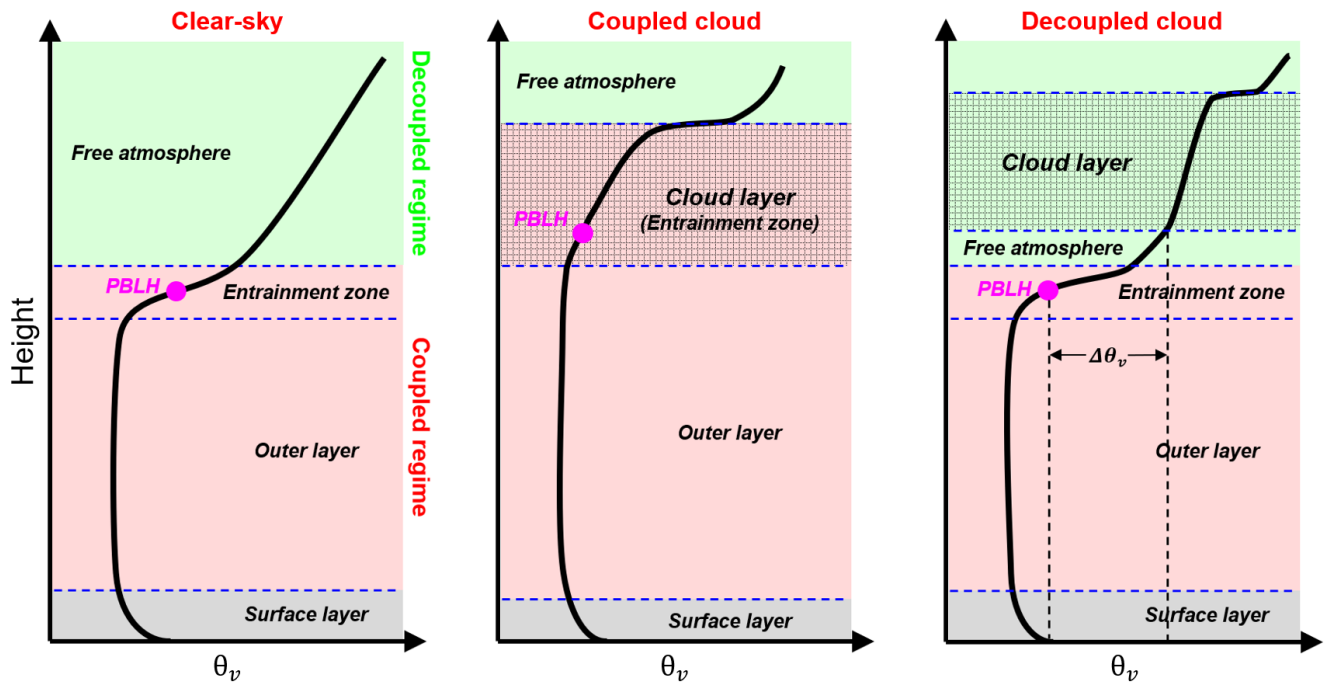
754

755

756

757

758

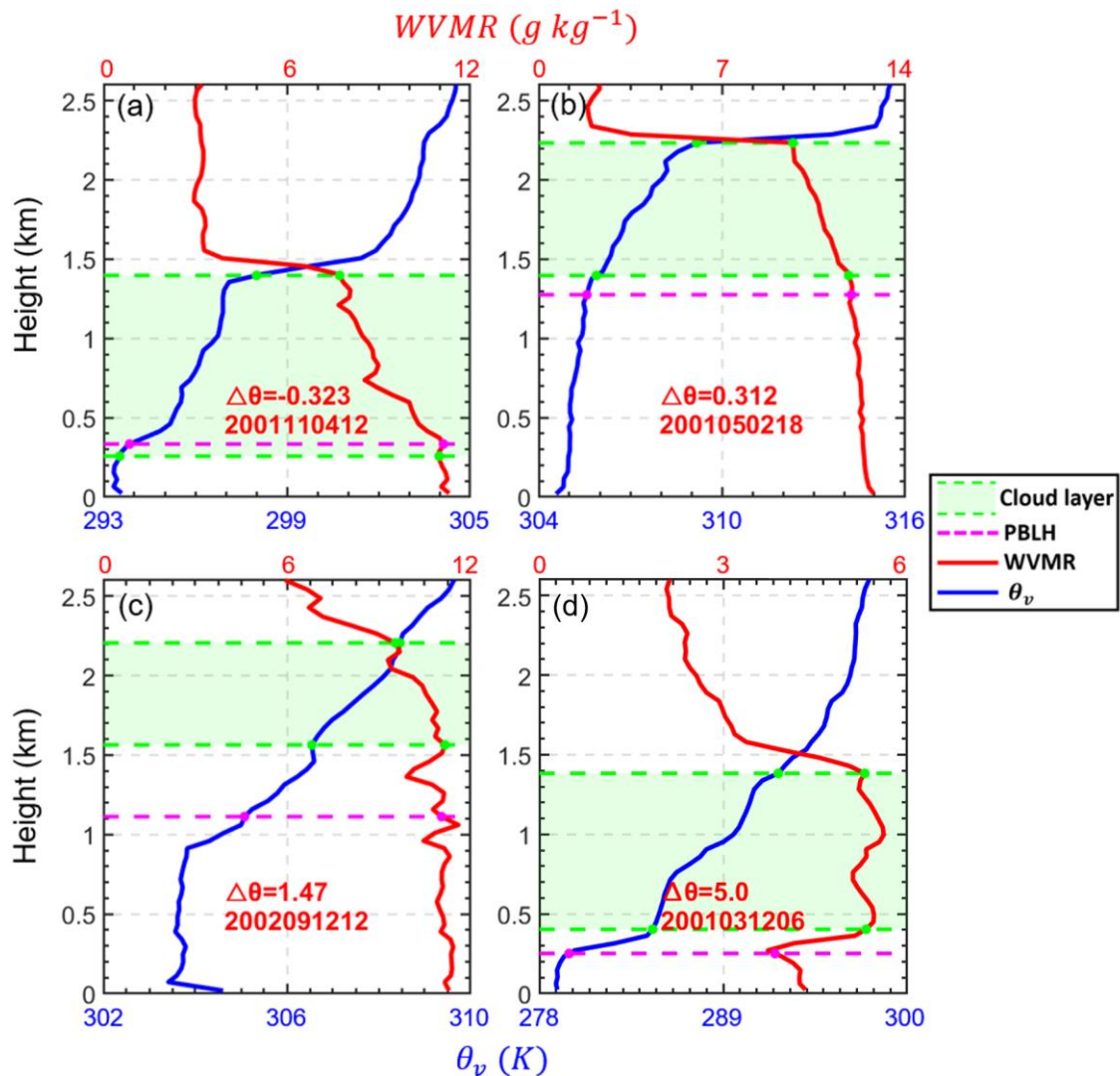


760

761 **Figure 1.** Idealized vertical profiles of virtual potential temperature (θ_v) under the clear-
 762 sky, coupled cloud, and decoupled cloud over land. The surface layer, outer layer
 763 entrainment zone, and free atmosphere are divided by the blue dash lines. The cloudy
 764 layer is marked as the shaded area, and PBLH is marked as the pink point. Red and
 765 green zones indicate the coupled and decoupled regime, respectively. Elements (e.g.,
 766 turbulence, heat fluxes, cloud) in the coupled regime are directly affected by the PBL
 767 processes, while these elements are not directly affected by the PBL processes in the
 768 decoupled regime. For the coupled cases, the cloud base is below the capping
 769 of entrainment zone. For the decoupled cases, the cloud base is above the capping
 770 inversion.

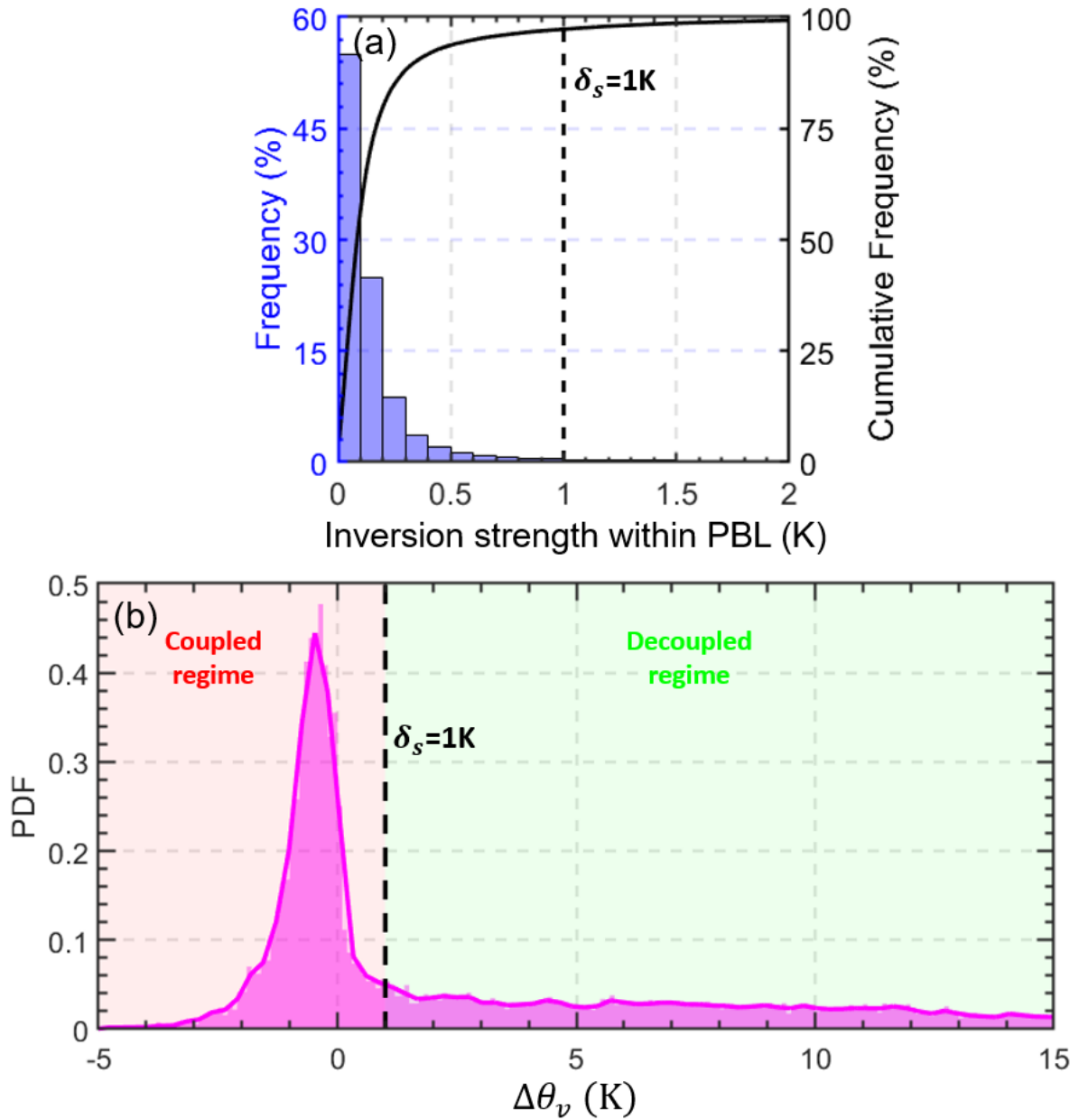
771

772



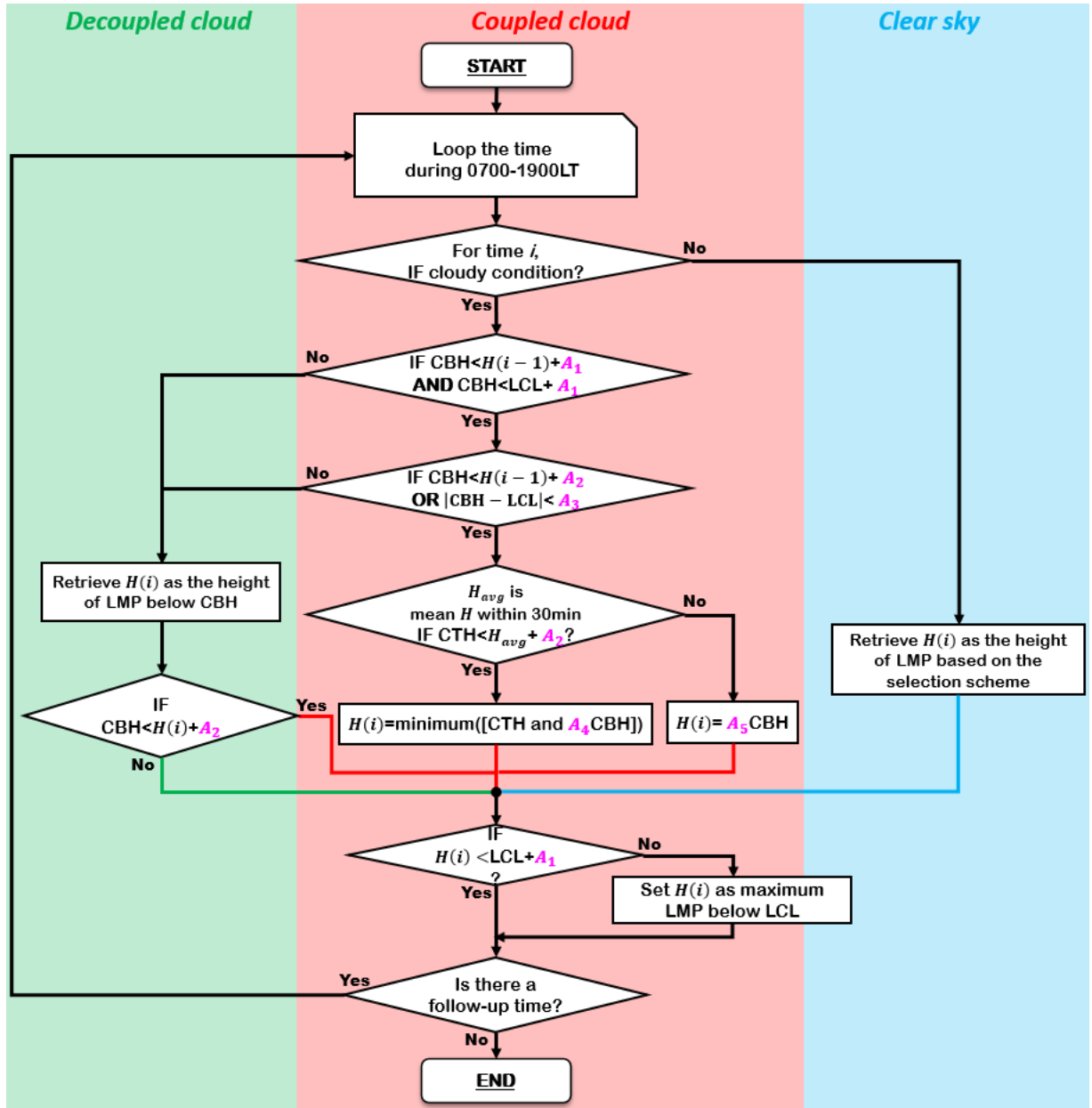
773

774 **Figure 2.** Virtual potential temperature (θ_v , blue lines) and water vapor mixing ratio
 775 (WVMR, red lines) profiles from radiosonde (RS) over the Southern Great Plains site
 776 for different cases. The differences in virtual potential temperature between the cloud
 777 base and the planetary boundary layer (PBL) top are expressed as $\Delta\theta_v$ ($\theta_v^{CBH} - \theta_v^{PBLH}$).
 778 The time of each radiosonde launch is marked in each panel as “YYYYMMDDHH”,
 779 where YYYY, MM, DD, and HH indicates the year, month, day, and local time,
 780 respectively. Green regions are cloud layers, and green dashed lines indicate their
 781 boundaries. The cloud layer is obtained from the CLDTYPE/ARSCL data. PBLHs is
 782 derived from RS data, and is marked as dashed pink lines.



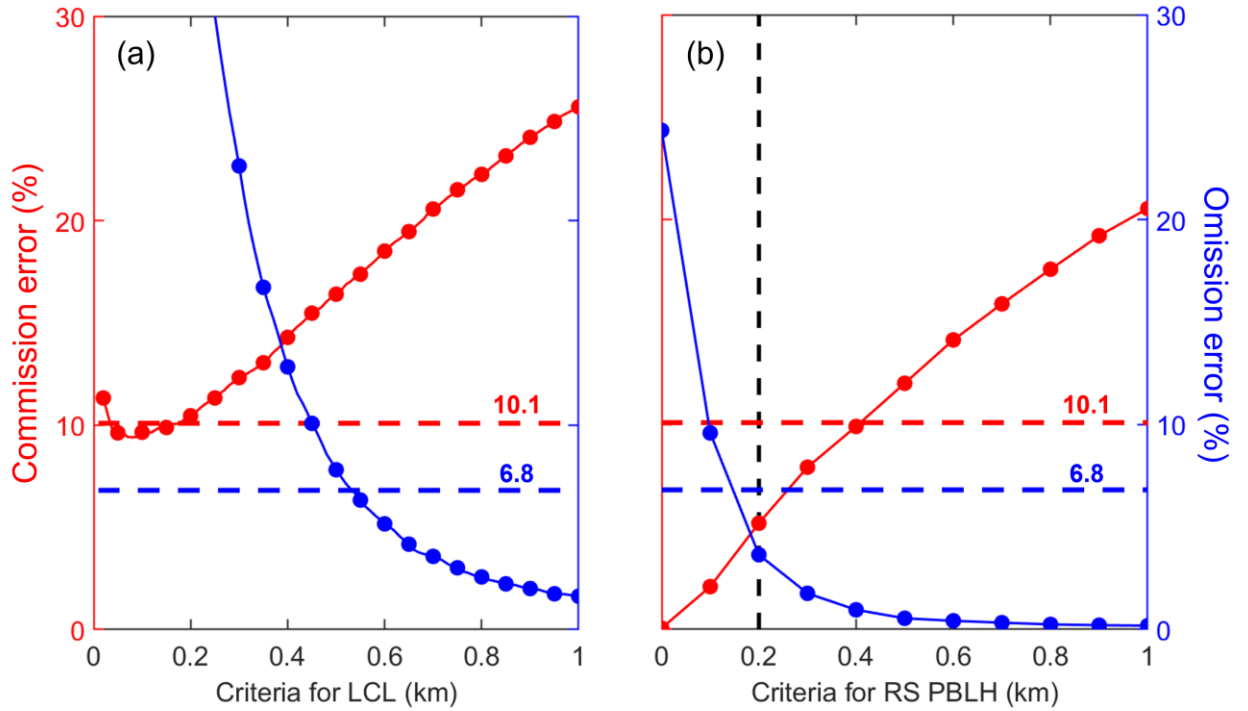
783

784 **Figure 3.** (a) Blue bars represent the inversion strength of θ_v within the PBL. The
 785 inversion strength is derived from the radiosonde during daytime (0800-1900LT). The
 786 inversions near surface or across PBL top are excluded. The black solid line represents
 787 cumulative frequency. (b) Pink area represents the probability density function (PDF)
 788 of the differences in the virtual potential temperature between cloud-base height (CBH)
 789 and PBLH ($\Delta\theta_v = \theta_v^{\text{CBH}} - \theta_v^{\text{PBLH}}$). By using a threshold of $\Delta\theta_v < \delta_s$ (1 K), we can
 790 identify the coupled cloud regime.



791

792 **Figure 4.** The flow chart of the updated DTDS algorithm. In this diagram, $H(i)$ is the
 793 retrieved planetary boundary layer height (PBLH) at time i . CBH and CTH represent
 794 the base and top heights, respectively, of the lowest cloud at time i . The PBLH part for
 795 selecting the suitable local maximum position (LMP) follows Su et al. (2020), and a
 796 detailed scheme for identifying a coupled cloud is added to the DTDS algorithm. LCL
 797 stands for lifted condensation level. Five empirical parameters (A_1, A_2, A_3, A_4, A_5) are
 798 set as 0.7, 0.2, 0.15, 1.35, 1.1, respectively.

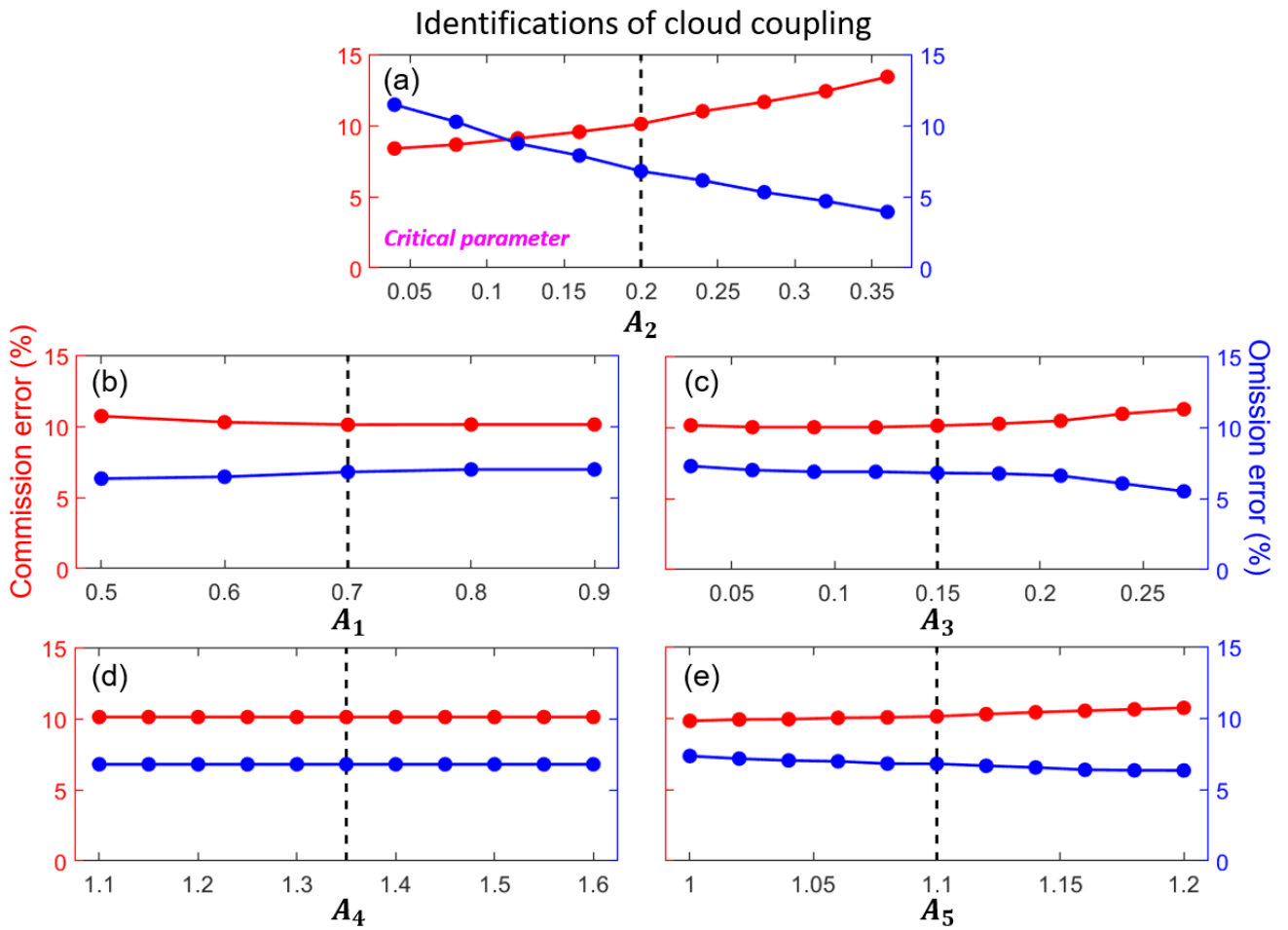


799

800 **Figure 5.** Commission errors and omission errors of coupled cloud identifications (a)
 801 for different criteria for the lifted condensation level (LCL) and (b) for different criteria
 802 for the planetary boundary layer height (PBLH). “Criteria for LCL” means coupled
 803 clouds are identified if $|CBH - LCL| < \text{Criteria for LCL}$. Similarly, “Criteria for RS
 804 PBLH” means coupled clouds are identified if $CBH - RS \text{ PBLH} < \text{Criteria for RS}$
 805 PBLH. The red and blue dashed lines indicate the commission and omission errors,
 806 respectively, for the DTDS algorithm. CBH stands for cloud-base height, and RS stands
 807 for radiosonde. By using ~ 7500 RS profiles, the cloud coupling state derived from the
 808 virtual potential temperature method (Section 3.1) is considered as the ground truth for
 809 evaluation.

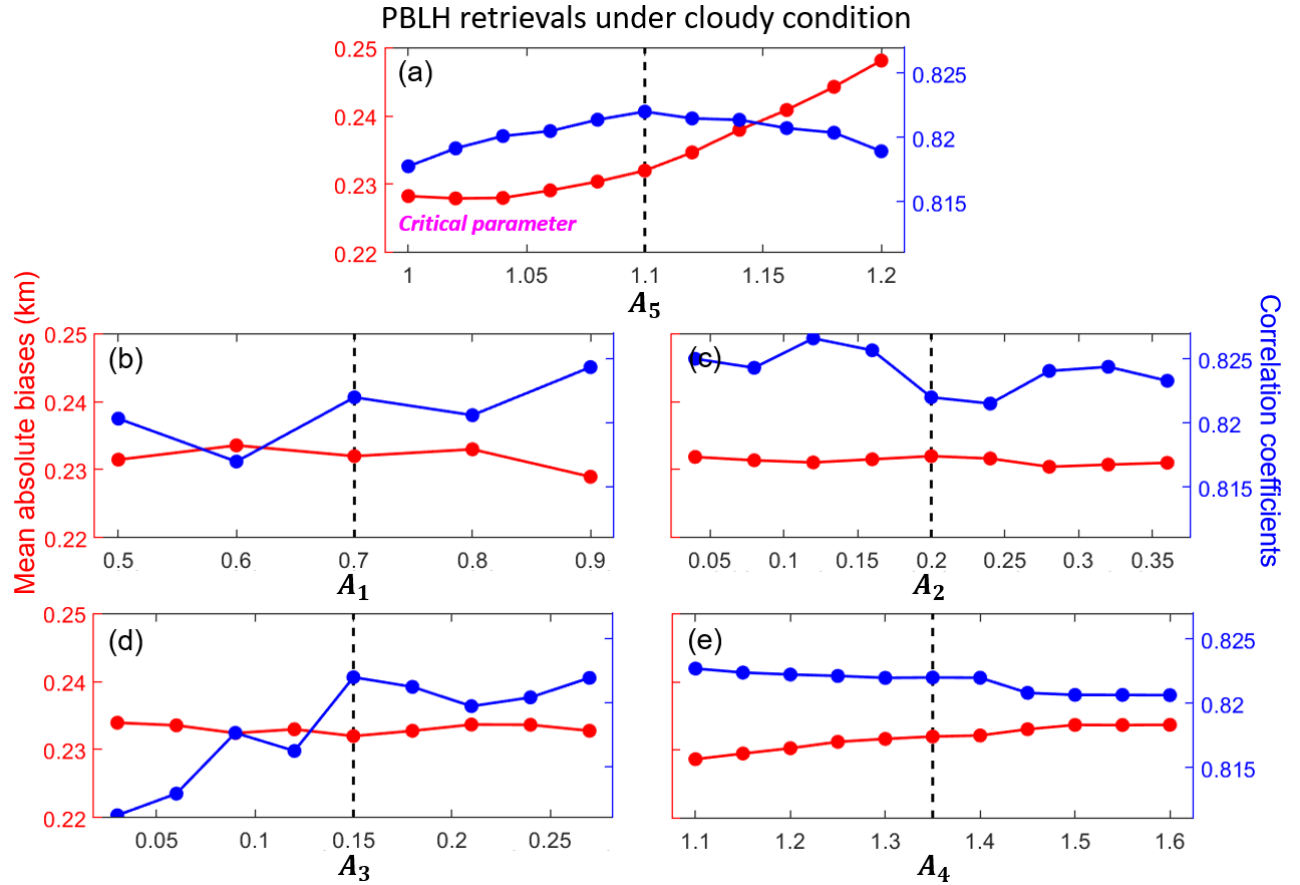
810

811



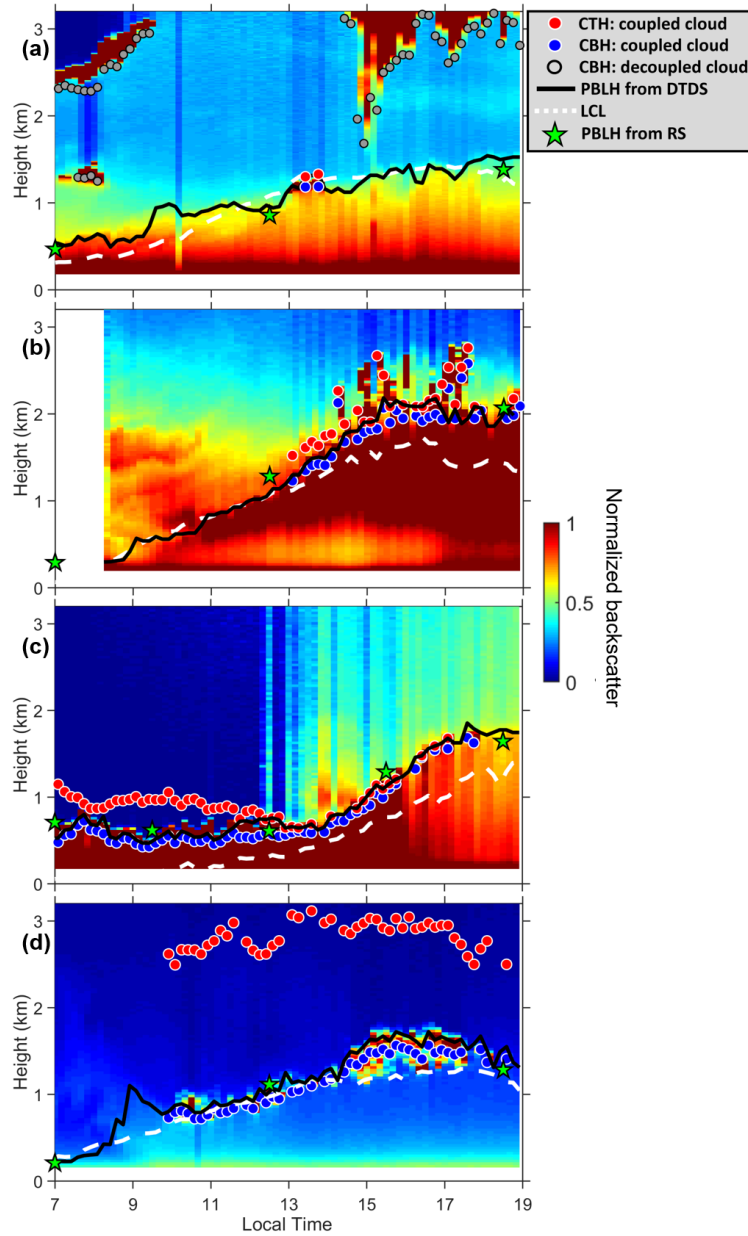
812

813 **Figure 6.** Commission errors (red line) and omission errors (blue line) of coupled cloud
 814 identifications for selecting different values of empirical parameters (A_1, A_2, A_3, A_4, A_5)
 815 in the DTDS algorithm. Black dash lines indicate the default values. For each test, one
 816 parameter is variable, while other parameters are set as default values. For
 817 identifications of cloud coupling, A_2 is the critical parameter.



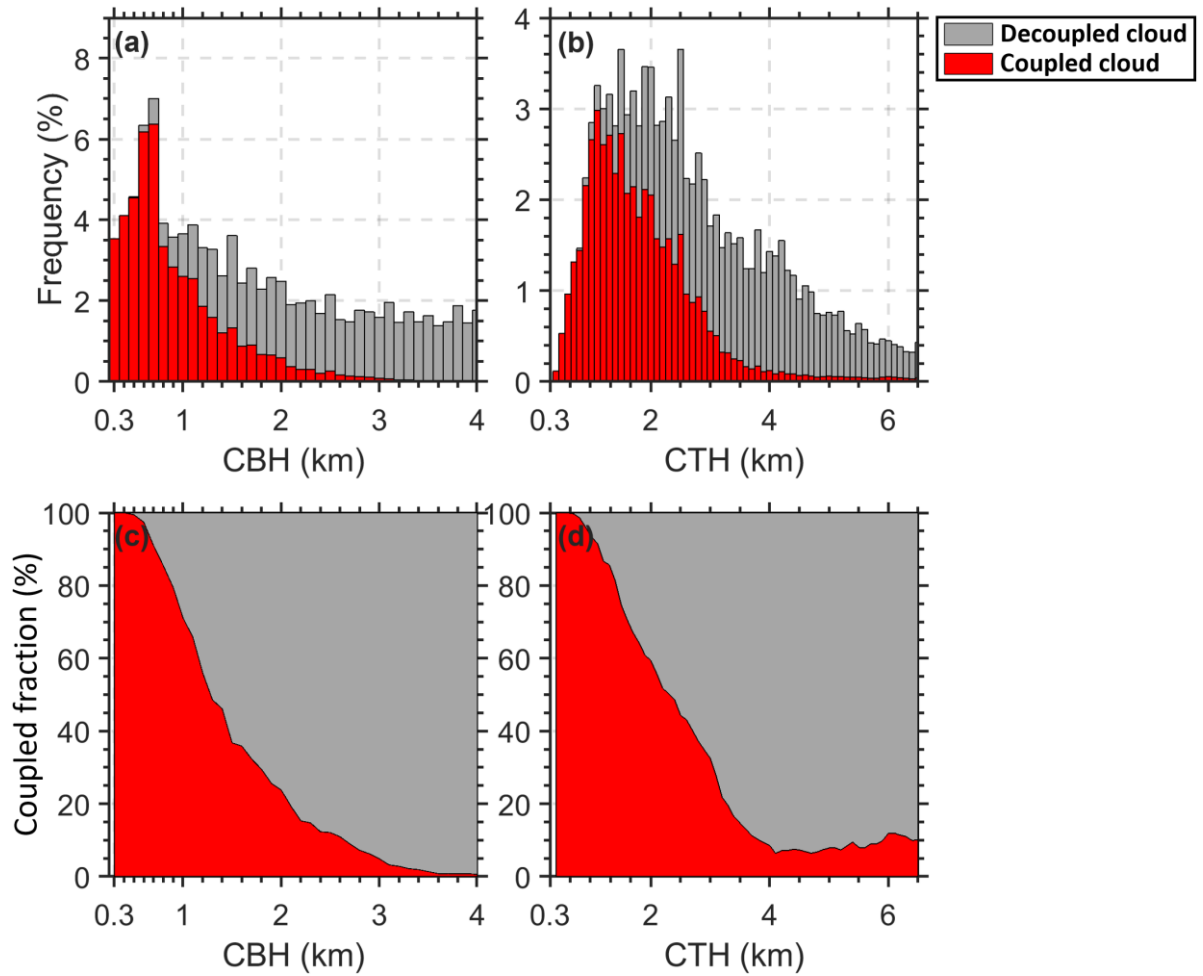
818

819 **Figure 7.** Red lines indicate the mean absolute biases between PBLH derived from lidar
 820 and radiosonde for selecting different values of empirical parameters (A_1, A_2, A_3, A_4, A_5)
 821 in the DTDS algorithm. Here, we only analyze the low cloud cases. Blue lines indicate
 822 the corresponding correlation coefficients between PBLH derived from lidar and
 823 radiosonde. Black dash lines indicate the default values. For each test, one parameter is
 824 variable, while other parameters are set as default values. For PBLH retrievals under
 825 cloudy conditions, A_5 is the critical parameter.



826

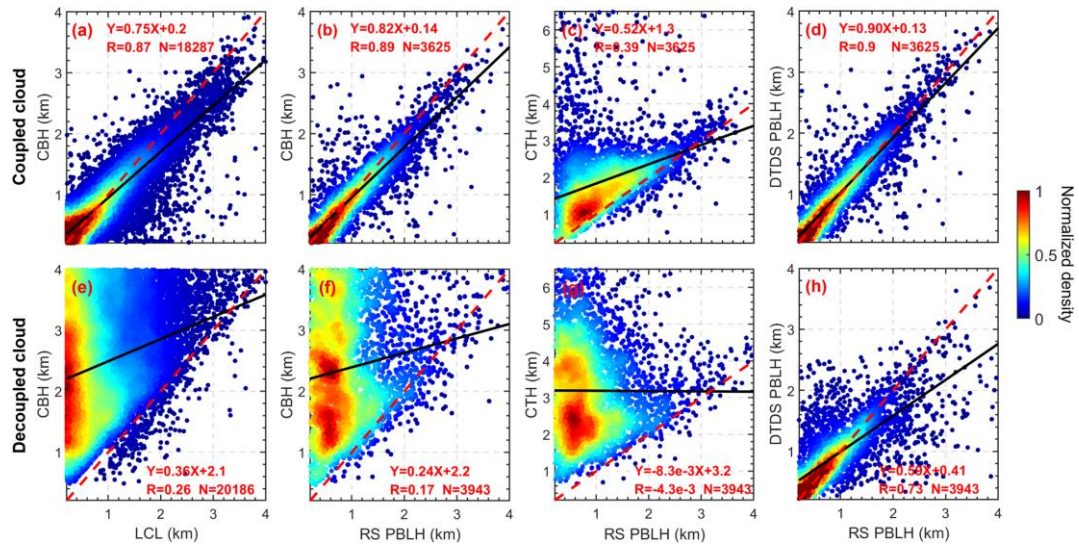
827 **Figure 8.** Daily backscatter profiles: (a) short-lived coupled cloud, (b) developed
 828 coupled cloud, (c) daylong coupled cloud, and (d) active coupled cloud. Backscatter is
 829 normalized to a range of 0–1 in arbitrary units. Red dots and blue dots indicate cloud-
 830 top heights (CTHs) and cloud-base heights (CBHs) of coupled clouds. Grey dots mark
 831 CBHs for decoupled clouds. Black lines and green stars mark the planetary boundary
 832 layer height (PBLH) retrieved from the DTDS algorithm and from radiosonde (RS)
 833 soundings, respectively. White dashed lines represent lifted condensation levels (LCLs).



834

835 **Figure 9.** The height-dependent occurrence frequencies of (a) the cloud-base height
 836 (CBH) and (b) the cloud-top height (CTH) for coupled clouds (red bars) and decoupled
 837 clouds (grey bars). The relative occurrence frequencies of (c) the CBH and (d) the CTH
 838 for coupled clouds (red area) and decoupled clouds (grey area).

839



840

841 **Figure 10.** The relationships between (a) LCL and CBH, (b) CBH and RS-derived
 842 PBLH, (c) CTH and RS-derived PBLH for coupled clouds, and (d) DTDS-derived
 843 PBLH and RS-derived PBLH. Panels (e-h) are similar to panels (a-d) but for decoupled
 844 clouds. Black lines represent the linear regressions. The linear fitting functions,
 845 correlation coefficients (R), and sampling numbers (N) are given in each panel.